

# The component masses of the cataclysmic variable V347 Puppis

T. D. Thoroughgood,<sup>1\*</sup> V. S. Dhillon,<sup>1</sup> D. Steeghs,<sup>2</sup> C. A. Watson,<sup>1</sup>  
 D. A. H. Buckley,<sup>3</sup> S. P. Littlefair,<sup>4</sup> D. A. Smith,<sup>1,5</sup> M. Still,<sup>6†</sup>  
 K. J. van der Heyden,<sup>3</sup> B. Warner<sup>7</sup>

<sup>1</sup>*Department of Physics and Astronomy, University of Sheffield, Sheffield, S3 7RH, UK*

<sup>2</sup>*Harvard-Smithsonian Center for Astrophysics, 60 Garden Street, MS-67, Cambridge, MA 02138, USA*

<sup>3</sup>*South African Astronomical Observatory, PO Box 9, Observatory 7935, Cape Town, South Africa*

<sup>4</sup>*School of Physics, University of Exeter, Stocker Road, Exeter, EX4, UK*

<sup>5</sup>*Winchester College, Winchester, SO23 9LX, UK*

<sup>6</sup>*NASA/Goddard Space Flight Center, Code 662, Greenbelt, MD 20771, USA*

<sup>7</sup>*Department of Astronomy, University of Cape Town, Private Bag, Rondebosch 7700, South Africa*

Accepted for publication in the Monthly Notices of the Royal Astronomical Society

7 December 2018

## ABSTRACT

We present time-resolved spectroscopy and photometry of the double-lined eclipsing cataclysmic variable V347 Pup (= LB 1800). There is evidence of irradiation on the inner hemisphere of the secondary star, which we correct for using a model to give a secondary star radial velocity of  $K_R = 198 \pm 5 \text{ km s}^{-1}$ . The rotational velocity of the secondary star in V347 Pup is found to be  $v \sin i = 131 \pm 5 \text{ km s}^{-1}$  and the system inclination is  $i = 84.0^\circ \pm 2.3^\circ$ . From these parameters we obtain masses of  $M_1 = 0.63 \pm 0.04 M_\odot$  for the white dwarf primary and  $M_2 = 0.52 \pm 0.06 M_\odot$  for the M0.5V secondary star, giving a mass ratio of  $q = 0.83 \pm 0.05$ . On the basis of the component masses, and the spectral type and radius of the secondary star in V347 Pup, we find tentative evidence for an evolved companion. V347 Pup shows many of the characteristics of the SW Sex stars, exhibiting single-peaked emission lines, high-velocity S-wave components and phase-offsets in the radial velocity curve. We find spiral arms in the accretion disc of V347 Pup and measure the disc radius to be close to the maximum allowed in a pressureless disc.

**Key words:** accretion, accretion discs – binaries: eclipsing – binaries: spectroscopic – stars: individual: V347 Pup – novae, cataclysmic variables.

## 1 INTRODUCTION

Cataclysmic variables (CVs) are close binary stars consisting of a red-dwarf secondary transferring material onto a white dwarf primary via an accretion disc or magnetic accretion stream. V347 Pup is an example of a nova-like variable (NL), a class of CV with high mass transfer rates and no recorded nova or dwarf-nova type outbursts; see Warner (1995a) for a comprehensive review of CVs.

A knowledge of the masses of the component stars in

CVs is fundamental to our understanding of the origin, evolution and behaviour of these systems. Population synthesis models (e.g. Kolb, King & Baraffe 2001) and the disrupted magnetic braking model of CV evolution (e.g. Spruit & Ritter 1983; Rappaport, Verbunt & Joss 1983) can be observationally tested only if the number of reliably known CV masses increases. One of the most reliable ways to measure the masses of CVs is to use the radial velocity and the rotational broadening of the secondary star in eclipsing systems. The radial velocity of the disc emission lines is often an unreliable indicator of the white dwarf motion because of contamination from, for example, the

\* E-mail: Tim.Thoroughgood@shef.ac.uk

† Also Universities Space Research Association

bright spot. At present, reliable masses are known for only  $\sim 20$  CVs, partly due to the difficulties in measurement (see Smith & Dhillon 1998 for a review).

V347 Pup was identified spectroscopically as a NL by Buckley et al. (1990) from the presence of high-excitation emission lines. Even though V347 Pup emits at X-ray wavelengths (as the *Uhuru* X-ray source 4U 0608–49), the NL classification was favoured over a magnetic CV class on account of the negligible polarisation present. The study by Buckley et al. (1990) revealed a bright and deeply eclipsing system, with a spectroscopic and photometric orbital period of 5.57 hrs. Their measured system inclination and emission-line radial velocity curve, together with an empirical secondary star mass estimated from the orbital period, suggested a high primary mass close to the Chandrasekhar limit.

A multiwavelength study by Mauche et al. (1994) revealed an X-ray spectral energy distribution similar to many dwarf novae in outburst, with a likely origin in an extended emission region rather than the boundary layer. The UV emission lines appear to have a similar origin and, in a later paper by Shlosman, Vitello & Mauche (1996), their behaviour in eclipse was successfully modelled as disc light scattered in a rotating wind. The presence of an accretion disc in V347 Pup was confirmed by a rotational disturbance of the optical emission lines through primary eclipse (Mauche et al. 1994; Still, Buckley & Garlick 1998). The latter authors found evidence for spiral arms and disc overflow accretion, and identified the low-excitation optical emission profiles as a composite of emission from the accretion disc and secondary star.

Secondary star absorption lines were found by Diaz & Hubeny (1999), who measured the system parameters of V347 Pup using the radial velocity semi-amplitudes of the primary and secondary stars. The radial velocity of the optical emission lines in V347 Pup varies widely in the literature, with published values of  $134 \pm 9 \text{ km s}^{-1}$  (Buckley et al. 1990),  $122 \pm 19 \text{ km s}^{-1}$  (Mauche et al. 1994),  $156 \pm 10 \text{ km s}^{-1}$ ,  $125 \pm 13 \text{ km s}^{-1}$  (Still, Buckley & Garlick 1998) and  $193 \pm 16 \text{ km s}^{-1}$  (Diaz & Hubeny 1999). The radial velocities of the UV emission lines published by Mauche et al. (1994) ranged between 220 and  $370 \text{ km s}^{-1}$  with large phase shifts between spectroscopic conjunction and photometric mid-eclipse. This wide range in values, and the known unreliability of using disc emission lines in NLs to determine the motion of the white dwarf (e.g. Dhillon, Marsh & Jones 1997), makes the determination of system parameters from the secondary star features alone highly desirable. In this paper, we derive the system parameters from the radial and rotational velocities of the secondary star in V347 Pup.

## 2 OBSERVATIONS AND REDUCTION

During January and December 1998 and January 1999, we obtained optical spectra of V347 Pup using the Cassegrain spectrograph + SITe1 CCD chip on the SAAO 1.9-m telescope. Simultaneous photometry was available for most of the spectra using the SAAO 1.0-m telescope with the TEK8 CCD chip. See Table 1 and its caption for full details.

On the December 1998 run, we observed 17 spectral

**Table 2.** Times of mid-eclipse for V347 Pup according to Buckley et al. (1990; B90), Baptista & Cieslinski (1991; BC91) and this paper.

Cycle (E)	HJD at mid-eclipse (2,400,000+)	Uncertainty on HJD	O–C (secs)	Reference
–4	46836.0379	$5 \times 10^{-4}$	335.96	B90
0	46836.9621	$5 \times 10^{-4}$	29.74	B90
39	46846.0059	$5 \times 10^{-4}$	–117.69	B90
43	46846.9333	$5 \times 10^{-4}$	–147.43	B90
48	46848.0930	$5 \times 10^{-4}$	–145.73	B90
56	46849.9500	$5 \times 10^{-4}$	–15.13	B90
65	46852.0373	$5 \times 10^{-4}$	–25.89	B90
69	46852.9651	$5 \times 10^{-4}$	–21.08	B90
78	46855.0533	$5 \times 10^{-4}$	45.92	B90
6177	48269.63136	$1.5 \times 10^{-4}$	48.28	BC91
7583	48595.73325	$1.1 \times 10^{-4}$	30.04	BC91
7587	48596.66022	$9 \times 10^{-5}$	–36.85	BC91
17179	50821.39199	$5 \times 10^{-4}$	56.29	This paper
17184	50822.55127	$5 \times 10^{-4}$	21.70	This paper
17192	50824.40676	$5 \times 10^{-4}$	21.83	This paper
17196	50825.33428	$5 \times 10^{-4}$	2.46	This paper
17197	50825.56611	$5 \times 10^{-4}$	–6.70	This paper
18697	51173.47035	$1 \times 10^{-4}$	6.20	This paper
18705	51175.32562	$1 \times 10^{-4}$	–12.68	This paper
18706	51175.55802	$1 \times 10^{-4}$	26.54	This paper
18710	51176.48519	$1 \times 10^{-4}$	–22.21	This paper

type templates ranging from G7V–M5.5V and telluric stars to remove atmospheric features. We observed flux standards on both the 1.9-m and 1.0-m telescopes on all nights.

The spectra and images were reduced using standard procedures (e.g. Dhillon, Jones & Marsh 1994; Thoroughgood et al. 2001). The photometry data were corrected for the effects of atmospheric extinction by subtracting the magnitude of a nearby comparison star. The absolute photometry is accurate to approximately  $\pm 0.5$  mJy; the relative photometry to  $\pm 0.01$  mag. Comparison arc spectra were taken every  $\sim 40$  min in order to calibrate the wavelength scale and instrumental flexure. The arcs were fitted with fourth-order polynomials with an rms scatter of better than  $0.04 \text{ \AA}$ . Where possible, slit losses were then corrected for by multiplying each V347 Pup spectrum by the ratio of the flux in the spectrum (over the whole spectral range) to the corresponding photometric flux.

## 3 RESULTS

### 3.1 Ephemeris

The times of mid-eclipse for V347 Pup were determined by fitting a parabola to the eclipse minima in the photometry data. A least-squares fit to the 21 eclipse timings listed in Table 2 yields the ephemeris:

$$T_{\text{mid-eclipse}} = \text{HJD } 2\,446\,836.96176 + 0.231936060 E \pm 0.00009 \pm 0.000000006. \quad (1)$$

Our new ephemeris is exactly the same as that given by Baptista & Cieslinski (1991), except we have reduced the errors on both the zero point and orbital period. We find no evidence for any systematic variation in the O–C values listed in Table 2.

**Table 1.** Journal of observations. During Jan 1998, we used Grating No. 4 to give a wavelength range of  $\sim 4200\text{--}5060\text{\AA}$  ( $\lambda_{cen} = 4610\text{\AA}$ ) at  $0.99\text{-\AA}$  ( $64\text{ km s}^{-1}$ ) resolution. Grating No. 4 was again used on 28 Dec 1998 and 23 Jan 1999 to give a wavelength range of  $\sim 4900\text{--}5720\text{\AA}$  ( $\lambda_{cen} = 5290\text{\AA}$ ) at  $0.95\text{-\AA}$  ( $54\text{ km s}^{-1}$ ) resolution. On 25 and 27 Dec 1998, we used Grating No. 5 to give a wavelength range of  $\sim 5960\text{--}6725\text{\AA}$  ( $\lambda_{cen} = 6330\text{\AA}$ ) at  $0.88\text{-\AA}$  ( $42\text{ km s}^{-1}$ ) resolution. Simultaneous photometry for the December 1998 spectra was recorded in the Johnson–Cousins  $V$  and  $R$  bands. Photometry was also available during the January 1998 run in the Strömgren  $b$  and  $y$  filters. The seeing measured around  $1.0$  arcsec with photometric conditions on 25 and 27 Dec 1998 and Jan 23 1999. On 28 Dec 1998, however, the seeing was poor and patchy high cloud was present. The seeing varied between  $1.0\text{--}1.5$  arcsec over the January 1998 run. The epochs are calculated using the new ephemeris presented in this paper (equation 1).

UT Date	1.9-m $\lambda_{cen}$ ( $\text{\AA}$ )	No. of spectra	Exposure time (s)	Epoch start	Epoch end	1.0-m filter	No. of images	Exposure time (s)	Epoch start	Epoch end
1998 Jan 07	4610	113	200	17178.62	17179.91	$b$	843	30	17178.88	17179.93
1998 Jan 08	4610	32	200	17182.88	17183.23	$b$	105	30	17183.83	17184.04
1998 Jan 10	4610	117	200	17191.94	17192.94	$y$	1379	30	17191.61	17192.96
1998 Jan 11	4610	129	200	17195.74	17197.25	$b$	1217	30	17195.81	17197.08
1998 Jan 12	4610	116	200	17200.09	17201.44	$b$	373	30	17200.14	17200.52
1998 Dec 25	6330	68	300	18696.47	18697.55	$R$	962	30	18696.32	18697.65
1998 Dec 27	6330	61	300	18705.18	18706.17	$R$	748	30	18704.95	18706.25
1998 Dec 28	5290	23	300	18709.63	18710.16	$V$	442	30	18709.50	18710.29
1999 Jan 23	5290	64	300	18821.30	18822.49		no photometry available			

### 3.2 Average spectrum

The average spectra of V347 Pup, uncorrected for orbital motion, are shown in Fig. 1. In Table 3, we list fluxes, equivalent widths and velocity widths of the most prominent lines measured from the average spectra.

The Balmer emission lines are broad, symmetric and single-peaked, instead of the double-peaked profile one would expect from a high inclination accretion disc (e.g. Horne & Marsh 1986). This behaviour is characteristic of the SW Sex stars (e.g. Dhillon, Marsh & Jones 1997). Previous studies of V347 Pup by Buckley et al. (1990) and Diaz & Hubeny (1999) agree with this single-peaked observation, however, the study by Still, Buckley & Garlick (1998) shows double-peaked low excitation lines (although this could be due to the presence of absorption cores). The HeI  $\lambda 6678\text{\AA}$  line appears to be composed of a narrow single-peaked component superimposed upon a broad double-peaked component. The other HeI emission lines can clearly be seen in the wavelength region centred on  $\lambda 4610\text{\AA}$  as double peaked in nature, with the possible exception of HeI  $\lambda 4471\text{\AA}$ . High-excitation emission is present through HeI  $\lambda 4686\text{\AA}$  and the CIII/NIII  $\lambda\lambda 4640\text{--}4650\text{\AA}$  Bowen fluorescence complex.

The secondary star is clearly visible in the average spectra as absorption lines of the neutral metals CaI, FeI and MgI, as seen in Diaz & Hubeny (1999). Secondary star features in the SW Sex stars are not unusual in the longer period systems, such as BT Mon (Smith, Dhillon & Marsh 1998), AC Cnc and V363 Aur (Thoroughgood et al. 2004).

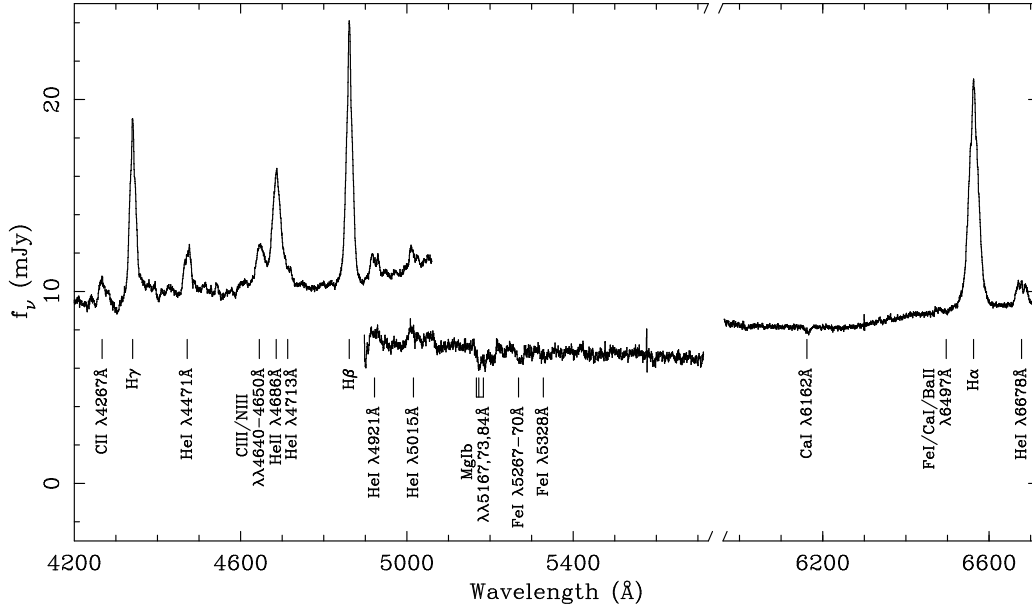
### 3.3 Light curves

Fig. 2 shows the broad-band and emission-line light curves of V347 Pup. The emission-line light curves were produced by subtracting a polynomial fit to the continuum and summing the residual flux. All light curves are plotted as a function of phase following the ephemeris derived in Section 3.1.

The  $b$ ,  $y$ ,  $V$  and  $R$ -band light curves show deep, asymmetrical primary eclipses with the egress lasting longer than ingress. Flickering is present in all light curves, as

well as an increase in brightness approaching eclipse in the  $b$ ,  $y$  and  $V$ -bands. The  $b$  and  $y$ -band data recorded in 1998 Jan show no significant brightness variations during the run, with out-of-eclipse magnitudes of  $13.3 \pm 0.1$  in both filters. The eclipse depths are 3.2 and 2.6 mag, respectively. We measure  $R$ -band out-of-eclipse magnitudes of  $14.00 \pm 0.05$  mag on Dec 25, increasing in brightness to  $13.45 \pm 0.10$  mag on Dec 27. The eclipse depth remains roughly the same at 2.1 mag and 2.0 mag, respectively. In the  $V$ -band, the out-of-eclipse magnitude is  $14.10 \pm 0.10$  mag, with an eclipse depth of 2.6 mag. Photometric out-of-eclipse magnitudes in the literature range between  $13.05\text{--}13.28$  in  $R$  and  $13.2\text{--}13.58$  in  $V$  (Buckley et al. 1990, Mauche et al. 1994), suggesting that our observations in Dec 1998 find V347 Pup around 0.5–1 mag fainter. Long-term variations in the magnitudes of NLs are not uncommon (e.g. Honeycutt 2001) and have been observed in other SW Sex stars (e.g. BH Lyn, Dhillon et al. 1992; DW UMa, Dhillon, Jones & Marsh 1994; PX And, Still, Dhillon & Jones 1995). Low states are often accompanied by the weakening or disappearance of the high-excitation HeII and CIII/NIII lines, which were unfortunately not observed in Dec 1998. There is, however, a change in the HeI  $\lambda 6678\text{\AA}$  Doppler maps between the two nights' observations, which is considered in Section 3.4. Further evidence that V347 Pup exhibits changes of state is seen in the EWs of the emission lines between the observed epochs. For example, the EW of H $\beta$  varies between  $17.0 \pm 0.6\text{\AA}$  (July 1986, Buckley et al. 1990),  $62.6 \pm 1.9\text{\AA}$  (April 1991, Mauche et al. 1994),  $9.8 \pm 0.1\text{\AA}$  (Jan 1995, Still, Buckley & Garlick 1998) and  $24.6 \pm 0.2\text{\AA}$  (Jan 1998, this paper), although the high-excitation CIII/NIII complex has a constant EW between epochs.

We measured the phase half-width of eclipse at the out-of-eclipse level ( $\Delta\phi$ ) by timing the first and last contacts of the eclipse and dividing by two. Our average value of  $\Delta\phi = 0.110 \pm 0.005$  is consistent with the values of  $0.120 \pm 0.011$  quoted by Harrop-Allin & Warner (1996) and  $0.105 \pm 0.005$  measured by Buckley et al. (1990). We then computed the radius of the accretion disc in V347 Pup using the geometric method outlined in Dhillon, Marsh & Jones (1991).



**Figure 1.** The average spectra for the three wavelength regions; the spectrum centred on  $\lambda 4610\text{\AA}$  is an average of all spectra recorded on the Jan 1998 run, and has not been corrected for slit-losses. The spectrum centred on  $\lambda 5290\text{\AA}$  is an average of all data recorded on 28 Dec 1998 and 23 Jan 1999, placed on an absolute flux scale (as determined from the 28 Dec 1998 photometry and flux standards). The spectrum centred on  $\lambda 6330\text{\AA}$  is composed of all data from 25 and 27 Dec 1998 and has been placed on an absolute flux scale. All average spectra are uncorrected for orbital motion, resulting in smeared spectral features.

**Table 3.** Fluxes and widths of prominent lines in V347 Pup, measured from the 2 nights' data centred on  $\lambda 6330\text{\AA}$  and the night of 11 Jan 1998 centred on  $\lambda 4610\text{\AA}$ . The full-width half-maximum (FWHM) velocities were determined from Gaussian fits, whereas the full-width zero-intensity (FWZI) velocities and their errors have been estimated by eye. HeII  $\lambda 4686\text{\AA}$ , CIII/NIII  $\lambda\lambda 4640-4650\text{\AA}$  and HeI  $\lambda 4713\text{\AA}$  are blended, so separate values of the flux and EW are given (determined from a triple-Gaussian fit) as well as the combined flux of the three.

Line	Date	Flux ( $\times 10^{-14}$ ergs cm $^{-2}$ s $^{-1}$ )	EW ( $\text{\AA}$ )	FWHM (km s $^{-1}$ )	FWZI (km s $^{-1}$ )
H $\alpha$	25 Dec 1998	$16.80 \pm 0.04$	$35.1 \pm 0.1$	$1100 \pm 100$	$3500 \pm 300$
H $\alpha$	27 Dec 1998	$27.98 \pm 0.05$	$36.4 \pm 0.1$	$1100 \pm 100$	$3600 \pm 300$
H $\beta$	11 Jan 1998	$42.2 \pm 0.1$	$24.6 \pm 0.2$	$1000 \pm 100$	$2800 \pm 300$
H $\gamma$	11 Jan 1998	$34.6 \pm 0.2$	$16.9 \pm 0.3$	$1100 \pm 100$	$2600 \pm 800$
HeI $\lambda 4471\text{\AA}$	11 Jan 1998	$8.0 \pm 0.1$	$3.8 \pm 0.2$	$1150 \pm 100$	$1850 \pm 200$
HeI $\lambda 4921\text{\AA}$	11 Jan 1998	$4.23 \pm 0.08$	$2.6 \pm 0.1$	$1300 \pm 100$	$2000 \pm 200$
HeI $\lambda 5015\text{\AA}$	11 Jan 1998	$3.3 \pm 0.1$	$2.2 \pm 0.2$	$1250 \pm 100$	$2000 \pm 200$
HeI $\lambda 6678\text{\AA}$	25 Dec 1998	$1.49 \pm 0.02$	$2.92 \pm 0.08$	$1250 \pm 100$	$1900 \pm 200$
HeI $\lambda 6678\text{\AA}$	27 Dec 1998	$2.40 \pm 0.04$	$3.00 \pm 0.08$	$1300 \pm 100$	$1900 \pm 200$
CII $\lambda 4267\text{\AA}$	11 Jan 1998	$3.8 \pm 0.1$	$1.7 \pm 0.4$	$900 \pm 200$	$1800 \pm 600$
HeII $\lambda 4686\text{\AA}$	11 Jan 1998	$26.9 \pm 0.3$	$13.1 \pm 0.3$	$1450 \pm 150$	
CIII/NIII $\lambda\lambda 4640-4650\text{\AA}$	11 Jan 1998	$11.7 \pm 0.1$	$6.4 \pm 0.2$	$1700 \pm 150$	
HeI $\lambda 4713\text{\AA}$	11 Jan 1998	$4.8 \pm 0.3$	$2.3 \pm 0.3$	$1500 \pm 300$	
HeI + CIII/NIII + HeI $\lambda 4713\text{\AA}$	11 Jan 1998	$45.5 \pm 0.2$	$22.4 \pm 0.2$		

Combining  $\Delta\phi$  with the system mass ratio and inclination derived in Section 3.10 gives an accretion disc radius ( $R_D$ ) of  $0.72 \pm 0.09 R_1$ , where  $R_1$  is the volume radius of the primary's Roche lobe. This value is in agreement with the value of  $R_D/R_1 \geq 0.82$  quoted by Harrop-Allin & Warner (1996) at the  $2\sigma$  level.

The H $\alpha$  eclipses are similar in shape to the continuum light curves, but do not appear to be as deeply eclipsed.

The H $\beta$  and H $\gamma$  lines exhibit asymmetric eclipses, with ingress longer than egress. This behaviour is expected from asymmetric disc emission, consistent with the spiral arms identified in the Doppler maps (Section 3.4). The high-excitation HeII + CIII/NIII complex has a deep and U-shaped eclipse, suggesting an origin close to the white dwarf. The HeI eclipses are wide with V-shaped minima, similar to the SW Sex stars (e.g. Knigge et al. 2000). Note that the

HeI flux is completely eclipsed, indicating an origin in the central portion of the disc, and not in an extended emission region which is larger than the secondary star. The HeI  $\lambda 4471\text{\AA}$  emission line shows a broad dip in flux around phase 0.4, before climbing to reach a maximum around phase 0.75, which could be a further signature of the disc asymmetry.

### 3.4 Trailed spectrum & Doppler tomography

We subtracted polynomial fits to the continuum and then rebinned the spectra onto a constant velocity–interval scale centred on the rest wavelength of the principal emission lines. For the data obtained in Jan 1998, we phase–binned all the spectra in order to boost the signal-to-noise (S/N). Individual spectra were weighted according to their S/N in order to optimally combine the spectra. The trailed spectra of H $\alpha$ , H $\beta$ , HeII  $\lambda 4686\text{\AA}$  and HeI  $\lambda\lambda 4471\text{\AA}$ ,  $5015\text{\AA}$ ,  $6678\text{\AA}$  are shown in Fig. 3. Doppler maps were calculated for the principal emission lines using the modulation Doppler tomography code of Steeghs (2003). This method is an extension to the conventional Doppler tomography technique (e.g. Marsh 2001), and maps both the constant and variable part of the line emission using a maximum–entropy regularised fitting procedure (Skilling & Bryan 1984). We found that the modulated contribution to the line emission was weak ( $< 1$  per cent), and thus our S/N was not sufficient to detect significant modulation in the accretion disc emission. We therefore plot in Fig. 4 the corresponding average Doppler maps only. The reconstructed line profiles are plotted next to the observed ones in Fig. 3 for comparison. Good fits to the data were achieved in all cases (reduced  $\chi^2 = 1 - 1.4$ )

The Balmer–line trailed spectra are dominated by a low–velocity component with a semi–amplitude of  $\sim 150 \text{ km s}^{-1}$ , moving from blue to red across primary eclipse. This is consistent with emission from the irradiated inner face of the secondary star, which is clearly seen in the corresponding Doppler maps. In the H $\beta$  map, a second low–velocity emission source is present, seemingly coincident with the gas stream at a distance of  $0.9L_1$ , where  $L_1$  is the distance from the white dwarf to the inner–Lagrangian point. There is also a weak two–armed disc asymmetry visible in the H $\beta$  emission, which is much more prominent in the double–peaked HeI emission lines. Doppler maps of V347 Pup have been produced by Still, Buckley & Garlick (1998) for data sets recorded in 1987, 1988 and 1995. The two components described above from the secondary star and the disc are clearly visible in their maps. The summed H $\beta$  and H $\gamma$  maps of Still, Buckley & Garlick (1998) show a stronger disc emission and spiral structure than our Balmer–line maps. The disc asymmetry is significant and is reminiscent of the two armed spiral structures that have been observed in the discs of dwarf novae during outburst (e.g. Steeghs 2001). We return to these in Section 4.1. The high–excitation HeII  $\lambda 4686\text{\AA}$  line is dominated by emission from the gas stream and bright spot overlaid on a weak accretion disc with radius  $R_D \sim 0.3 - 0.4L_1$ . Note that the HeII  $\lambda 4686\text{\AA}$  Doppler map shows emission at higher velocities than the low–excitation lines, demonstrating that the material originates from closer to the white dwarf.

The blue and red HeI emission lines were recorded almost a year apart and exhibit clear differences in structure.

The secondary star emission is clearly evident in HeI  $\lambda 6678\text{\AA}$  (Dec 1998), although no strong HeI  $\lambda 4471\text{\AA}$  or  $\lambda 5015\text{\AA}$  emission can be seen in the Jan 1998 data. There is also a difference in the HeI  $\lambda 6678\text{\AA}$  Doppler maps between the 25th and 27th Dec 1998, which is probably related to the change in brightness of the system; the 25th Dec 1998 Doppler map has more enhanced spiral features and weaker secondary star emission than the 27th Dec (note that the average map of these two nights is shown in Fig. 4). During all these epochs, however, the spiral structures were observed, demonstrating that they are a persistent feature.

### 3.5 Radial velocity of the white dwarf

We measured the radial velocities of the emission lines in V347 Pup by applying the double–Gaussian method of Schneider & Young (1980), since this technique is sensitive mainly to the line wings and should therefore reflect the motion of the white dwarf with the highest reliability. We tried Gaussians of widths 200, 300 and  $400 \text{ km s}^{-1}$  and we varied their separation from 200 to  $3200 \text{ km s}^{-1}$ . We then fitted

$$V = \gamma - K \sin[2\pi(\phi - \phi_0)] \quad (2)$$

to each set of measurements, where  $V$  is the radial velocity,  $K$  the semi–amplitude,  $\phi$  the orbital phase, and  $\phi_0$  is the phase at which the radial velocity curve crosses from red to blue. Examples of the radial velocity curves measured for the H $\alpha$ , H $\beta$ , HeII  $\lambda 4686\text{\AA}$  and HeI  $\lambda 4471\text{\AA}$  emission lines are shown in Fig. 5. There is clear evidence of rotational disturbance in the emission lines, where the radial velocities measured just prior to eclipse are skewed to the red, and those measured after eclipse are skewed to the blue. This confirms the detection of a similar feature in the trailed spectra, and indicates that at least some of the emission must originate in the disc. There is also evidence of a phase shift in H $\alpha$  and HeII  $\lambda 4686\text{\AA}$ , where the spectroscopic conjunction of each line occurs after photometric mid–eclipse. This phase shift implies an emission–line source trailing the accretion disc, such as a bright spot, and is a common feature of SW Sex stars (e.g. DW UMa, Shafter, Hessman & Zhang 1988; V1315 Aql, Dhillon, Marsh & Jones 1991; SW Sex, Dhillon, Marsh & Jones 1997). There appear to be no significant phase shifts, however, in the other emission lines. Buckley et al. (1990), Mauche et al. (1994) and Diaz & Hubeny (1999) find no evidence of phase shift in any of their emission lines, although their errors on  $\phi_0$  were much larger.

We tried to measure white dwarf radial velocity ( $K_W$ ) values using a diagnostic diagram (Shafter, Szkody & Thorstensen 1986), but with no success. We therefore attempted to make use of the light–centres method, as described by Marsh (1988). In the co–rotating co–ordinate system, the white dwarf has velocity  $(0, -K_W)$ , and symmetric emission, say from a disc, would be centred at that point. By plotting  $K_x = -K \sin \phi_0$  versus  $K_y = -K \cos \phi_0$  for the different radial velocity fits (Fig. 6), one finds that the points move closer to the  $K_y$  axis with increasing Gaussian separation. A simple distortion which only affects low velocities, such as a bright spot, would result in this pattern, equivalent to a decrease in distortion as one measures emission further into the line

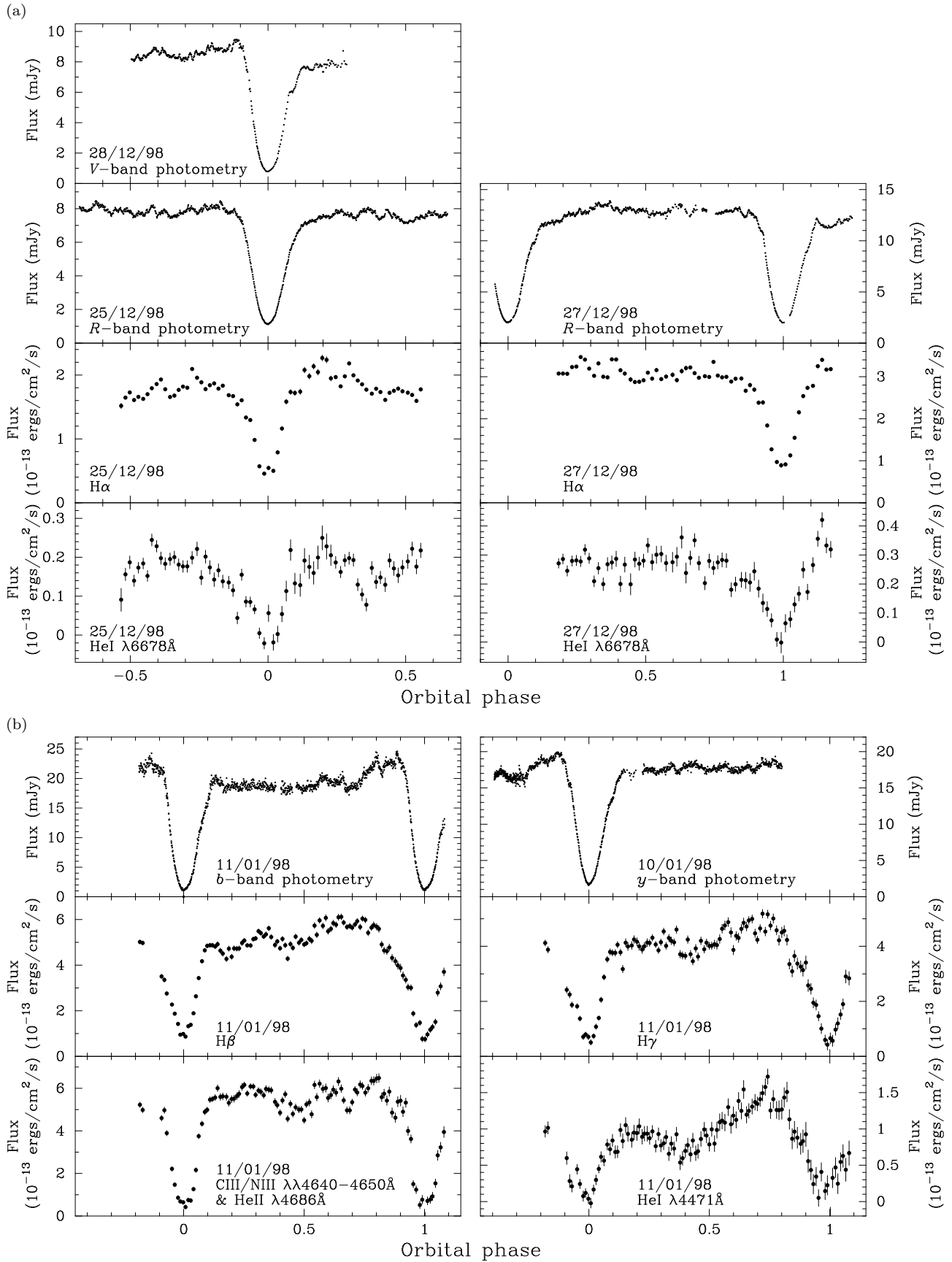


**Figure 2.** Broad-band and emission-line light curves of V347 Pup recorded in Dec 1998 and Jan 1999 (a), and Jan 1998 (b); see the panel labels for details. Note the increase in continuum and emission-line flux between Dec 25 and Dec 27 1998.

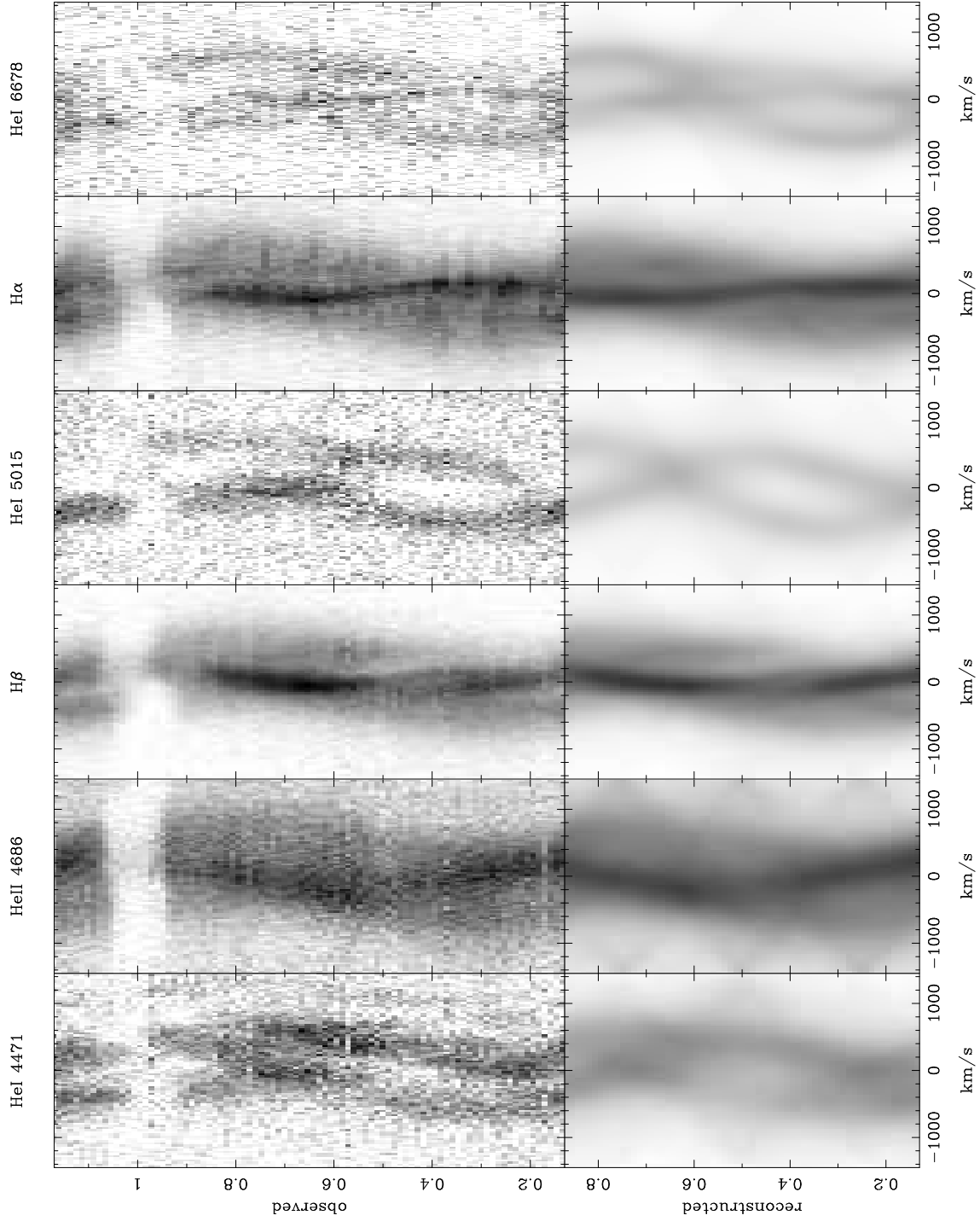


**Figure 3.** Trained spectra and data computed from the Doppler maps (Fig. 4). The blue data recorded in Jan 1998 have been phase binned into 200s bins, the red data recorded in Dec 1998 into 300s bins.  $H\gamma$  has not been shown, as it is very similar in nature to  $H\beta$ .

wings and therefore more closely representing the velocity of the primary star. By linearly extrapolating the largest Gaussian separation on the  $H\alpha$  light-centre diagram to the  $K_y$  axis, we measure the radial velocity semi-amplitude of the white dwarf to be  $\sim 180 \text{ km s}^{-1}$ . The large uncertainty in this value ( $\sim 40 \text{ km s}^{-1}$ ), however, and the unsuccessful application of the technique to the other emission lines,

prompted us to proceed with the mass determination using the secondary star features alone.

### 3.6 Radial velocity of the secondary star

The secondary star in V347 Pup is clearly visible in Fig. 1 through absorption lines of MgI, FeI and CaI. We compared regions of the spectra rich in absorption lines with a num-

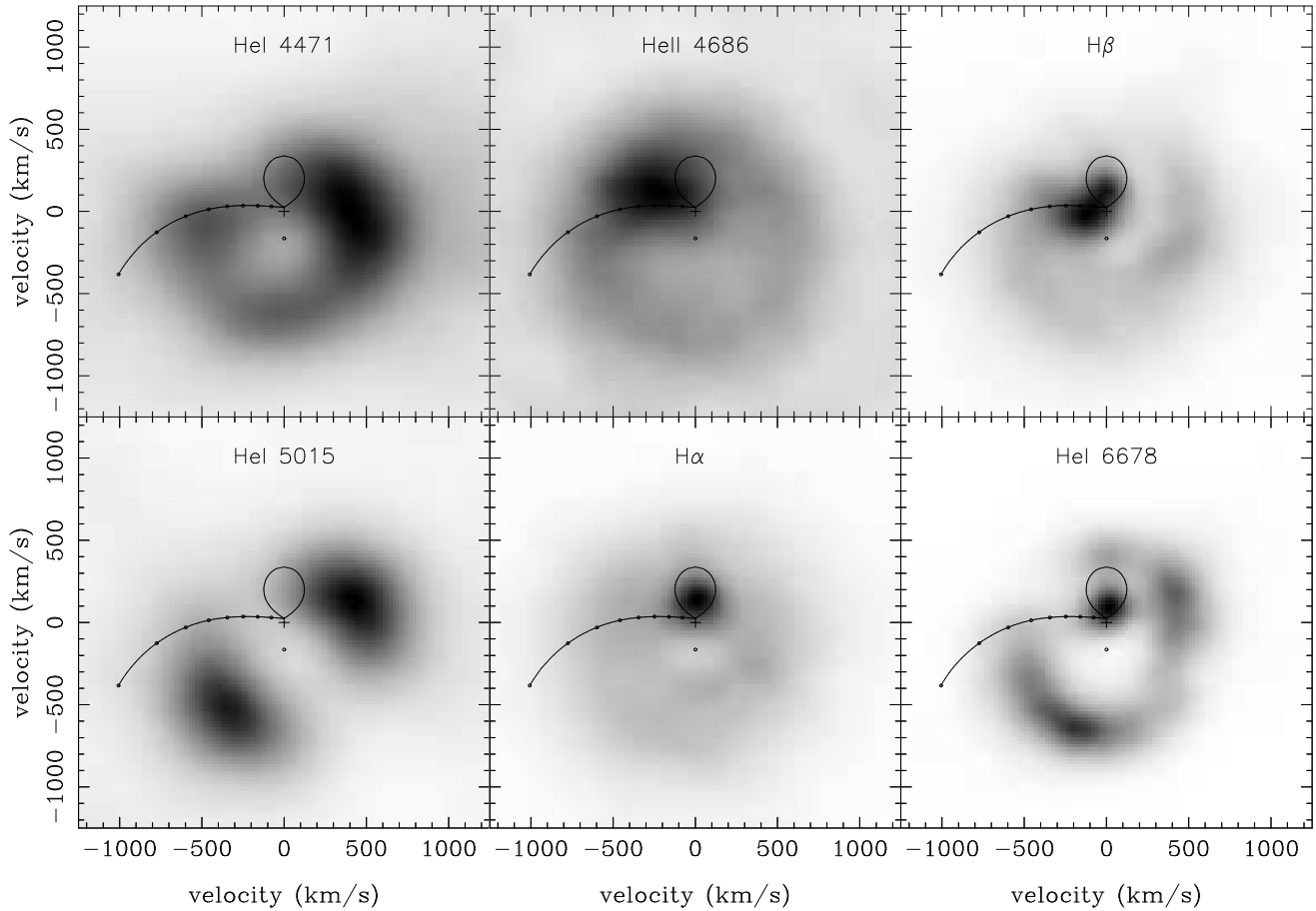


**Figure 4.** Doppler maps of the principal emission lines ( $H\gamma$  is not shown, as it is very similar in nature to  $H\beta$ ). The cross marked on each Doppler map represents the centre of mass of the system and the open circle represents the white dwarf. These symbols, the Roche lobe of the secondary star and the predicted trajectory of the gas stream, have been plotted using the  $K_R$ -corrected system parameters summarised in Table 5. The series of points along the gas stream mark the distance from the white dwarf at intervals of  $0.1L_1$ , ranging from  $1.0L_1$  at the red star to  $0.2L_1$ . Doppler tomography cannot properly account for variable line flux, so spectra around primary eclipse were omitted from the fits.

ber of templates with spectral types G7V–M3.5V. A technique known as skew mapping was used to enhance the secondary features and obtain a measurement of the radial velocity semi-amplitude of the secondary star ( $K_R$ ). See Vande Putte et al. (2003) for a detailed critique of skew mapping and Thoroughgood et al. (2004) for a successful application to AC Cnc and V363 Aur.

The data centred on  $\lambda 5290\text{\AA}$  were recorded specifically to exploit the secondary star features found between the  $H\beta$  and  $H\alpha$  lines. Unfortunately, the presence of weak emission lines (e.g. FeII multiplet 42 at  $\lambda\lambda 4924\text{\AA}$ ,  $5018\text{\AA}$  and  $5169\text{\AA}$ , Mason & Howell 2003) hampered all efforts to determine a  $K_R$  value from these data. The dominance of the emission lines in the spectra centred on  $\lambda 4610\text{\AA}$  also prevented a  $K_R$  determination from these data. The red spectra of V347 Pup centred on  $\lambda 6330\text{\AA}$ , however, allowed us to study the secondary star through absorption features blueward of  $H\alpha$ , such as the CaI  $\lambda 6162\text{\AA}$  line. Exactly the same conclusion was reached by Diaz & Hubeny (1999).

The first step was to shift the spectral type template stars to correct for their radial velocities. We then normalized each spectrum by dividing by a constant and then sub-

tracting a polynomial fit to the continuum. This ensures that line strength is preserved along the spectrum. The V347 Pup spectra were normalized in the same way. The template spectra were artificially broadened to account for both the orbital smearing of the V347 Pup spectra due to their exposure times ( $t_{exp}$ ), using the formula

$$V = \frac{t_{exp} 2\pi K_R}{P} \quad (3)$$

(e.g. Watson & Dhillon 2001), and the rotational velocity of the secondary ( $v \sin i$ ). Estimated values of  $K_R$  and  $v \sin i$  were used in the first instance, before iterating to find the best-fitting values given in Section 3.10. Regions of the spectrum devoid of emission lines were then cross-correlated with each of the templates, yielding a time series of cross-correlation functions (CCFs) for each template star. The regions used for the cross-correlation can be seen in Fig. 8. To produce the skew maps, these CCFs were then back-projected in the same way as time-resolved spectra in standard Doppler tomography (Marsh & Horne 1988). If there is a detectable secondary star, we expect a peak at  $(0, K_R)$  in the skew map. This can be repeated for each of the tem-



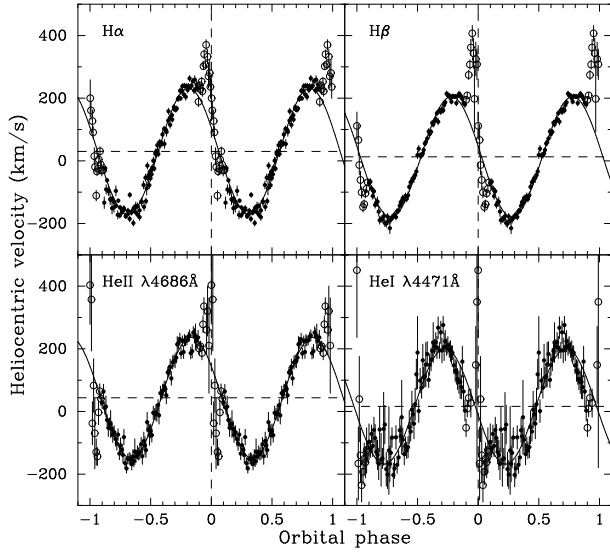


**Figure 5.** Radial velocity curves of  $H\alpha$ ,  $H\beta$ ,  $\text{HeII } \lambda 4686\text{\AA}$  and  $\text{HeI } \lambda 4471\text{\AA}$  using Gaussian widths of  $300 \text{ km s}^{-1}$  and a separation of  $1400 \text{ km s}^{-1}$ . We omitted the points around primary eclipse during the fitting procedure (open circles) as these measurements are affected by the rotational disturbance. The emission lines recorded in Jan 1998 have been phase-binned into 100 bins for clarity.

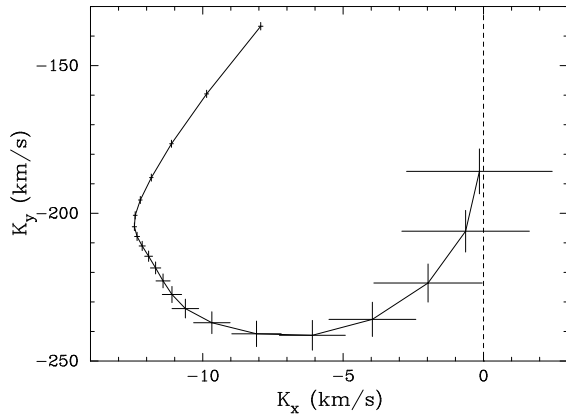


**Figure 6.** Light-centres diagram for  $H\alpha$ . Points are plotted for radial velocity fits using Gaussians of  $\text{FWHM} = 300 \text{ km s}^{-1}$ , with separations from  $900 \text{ km s}^{-1}$  to  $2900 \text{ km s}^{-1}$  at  $100 \text{ km s}^{-1}$  intervals. The points move anti-clockwise, towards the  $K_x = 0$  axis with increasing Gaussian separation.

plates, and the final skew map is the one that gives the strongest peak.

The skew maps show well-defined peaks at  $K_y \approx 216 \text{ km s}^{-1}$  – the skew map of the M0.5V template is shown in Fig. 7 together with the trailed CCFs. A systemic velocity of  $\gamma = 15 \text{ km s}^{-1}$  was applied in order to shift the skew map peaks onto the  $K_x = 0$  axis (see Smith, Dhillon & Marsh 1998 for details). We therefore adopt  $\gamma = 15 \pm 5 \text{ km s}^{-1}$  as the systemic velocity of V347 Pup, in excellent agreement with the values of  $16 \pm 10 \text{ km s}^{-1}$  and  $15 \pm 12 \text{ km s}^{-1}$  measured by Still, Buckley & Garlick (1998) from the Balmer and  $\text{HeII } \lambda 4686\text{\AA}$  emission lines. The  $\gamma$  velocities from

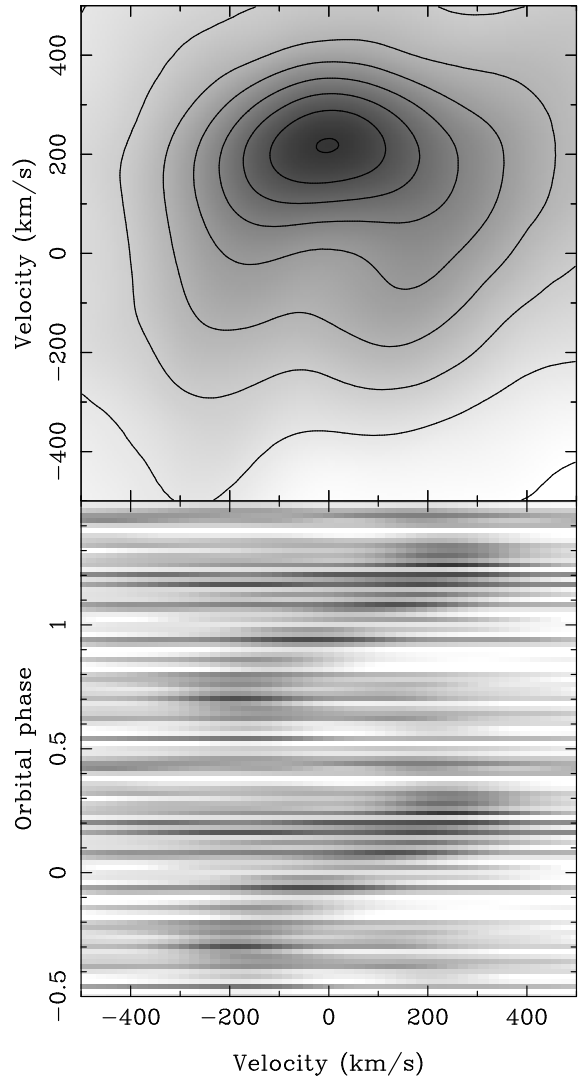


**Figure 7.** Skew maps (top) and trailed CCFs (bottom) of V347 Pup cross-correlated with a M0.5V dwarf template.

the emission lines shown in Fig. 5 ranged between  $13 \text{ km s}^{-1}$  and  $44 \text{ km s}^{-1}$ . Other  $\gamma$  values measured from optical emission lines vary widely in the literature ( $-3$  to  $60 \text{ km s}^{-1}$ , Diaz & Hubeny 1999;  $-9$  to  $159 \text{ km s}^{-1}$ , Mauche et al. 1994).

Our adopted  $K_R$  of  $216 \pm 5 \text{ km s}^{-1}$  was derived from the skew map peak of the best-fitting template found in Section 3.10. This result actually covers the  $K_R$  values derived from *all* of the template stars to within the errors, demonstrating that the result is robust to the choice of template (see Table 4).

### 3.7 Rotational velocity and spectral type of the secondary star

The spectral-type templates were broadened for smearing due to orbital motion, as before, and rotationally broadened by a range of velocities ( $50$ – $240 \text{ km s}^{-1}$ ). We then ran an optimal subtraction routine, which subtracts a constant times the normalized template spectrum from the normalized aver-

**Table 4.**  $v \sin i$  values for V347 Pup cross-correlated with the rotationally broadened profiles of G7 – M3.5V templates. Also shown is the factor used to multiply the template star features during optimal extraction, and the position of the strongest peak in the skewmaps derived from each template using  $\gamma$ -velocities of 0 km s<sup>-1</sup> and 15 km s<sup>-1</sup>.

Templates	$v \sin i$ at min $\chi^2$ (km s <sup>-1</sup> )	Optimal factor	$(K_x, K_y)$ $\gamma = 0$ (km s <sup>-1</sup> )	$(K_x, K_y)$ $\gamma = 15$ (km s <sup>-1</sup> )
G7V	134	0.32 ± 0.05	(-26,212)	(10,220)
G9V	133	0.28 ± 0.04	(-13,215)	(13,220)
K0V	133	0.23 ± 0.03	(-2,217)	(14,219)
K1V	134	0.24 ± 0.03	(-15,215)	(8,220)
K2V	133	0.20 ± 0.03	(-22,212)	(6,219)
K3V	136	0.19 ± 0.03	(-28,212)	(0,217)
K4V	135	0.14 ± 0.02	(-17,211)	(3,217)
K5V	134	0.13 ± 0.02	(-17,213)	(1,218)
K7V	133	0.12 ± 0.02	(-24,210)	(-3,216)
M0.5V	130	0.13 ± 0.02	(-18,213)	(0,216)
M1.5V	125	0.12 ± 0.02	(-17,213)	(-2,216)
M2.5V	126	0.13 ± 0.02	(-21,213)	(-7,216)
M3.5V	127	0.12 ± 0.02	(-33,213)	(-23,217)

age V347 Pup spectrum, adjusting the constant to minimize the scatter in the residual. (Normalisation was carried out in the same way as Section 3.6, except that this time, the spectra were set to unity.) The scatter is measured by carrying out the subtraction and then computing the  $\chi^2$  between the residual spectrum and a smoothed version of itself. By finding the value of rotational broadening that minimizes the  $\chi^2$ , we obtain an estimate of both  $v \sin i$  and the spectral type of the secondary star. Note that the  $v \sin i$  values of the template stars are much lower than the instrumental resolution, so do not affect our measurements of  $v \sin i$  for the secondary star.

The value of  $v \sin i$  obtained using this method varies depending on the spectral type template, the wavelength region for optimal subtraction, the amount of smoothing of the residual spectrum in the calculation of  $\chi^2$  and the value of the limb-darkening coefficient used in the broadening procedure. The values of  $v \sin i$  for all of the templates calculated using values for the limb-darkening coefficient of 0.5 and smoothed using a Gaussian of FWHM = 15 km s<sup>-1</sup>, are listed in Table 4.

A plot of  $\chi^2$  versus  $v \sin i$  for each spectral-type template is shown in Fig. 9. The spectral type with the lowest  $\chi^2$  value is M0.5V, which agrees with a visual identification of the best fitting template. Diaz & Hubeny (1999), however, estimate a secondary star spectral type between K0V and K5V, with the possibility of a later-type subgiant. A plot of the V347 Pup average spectrum, a broadened M0.5V template spectrum and the residual of the optimal subtraction is shown in Fig. 8. The  $\chi^2$  for the M0.5V template has a minimum at 130 km s<sup>-1</sup>, so we adopt  $v \sin i = 130 \pm 5$  km s<sup>-1</sup>, with the error accounting for the measurement accuracy and the other variables noted in the previous paragraph. The error quoted on our adopted value encompasses the measured  $v \sin i$  for all of the templates used in the analysis (except for K3V with  $v \sin i = 136$  km s<sup>-1</sup>).

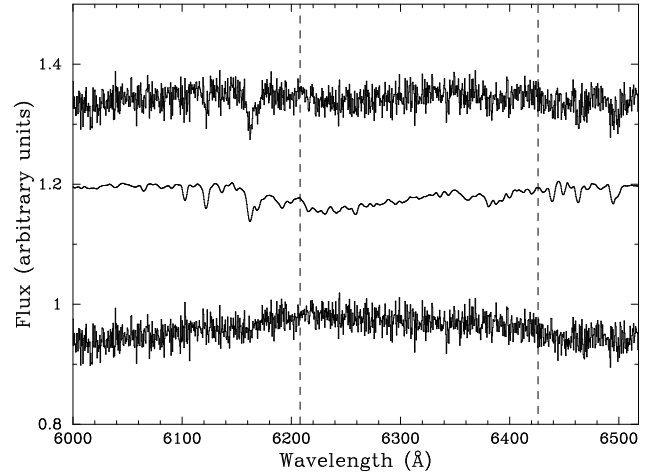


**Figure 8.** Orbitally-corrected average spectrum of V347 Pup (top) with the broadened M0.5V template (middle) and the residuals after optimal subtraction (bottom). The template spectrum has been multiplied by the scaling factor found from the optimal subtraction. All of the spectra are normalised and offset on the plot by an arbitrary amount for clarity. The wavelength limits shown are those used for the cross-correlation and optimal subtraction procedures, except for the region between the dashed lines owing to few secondary star features.

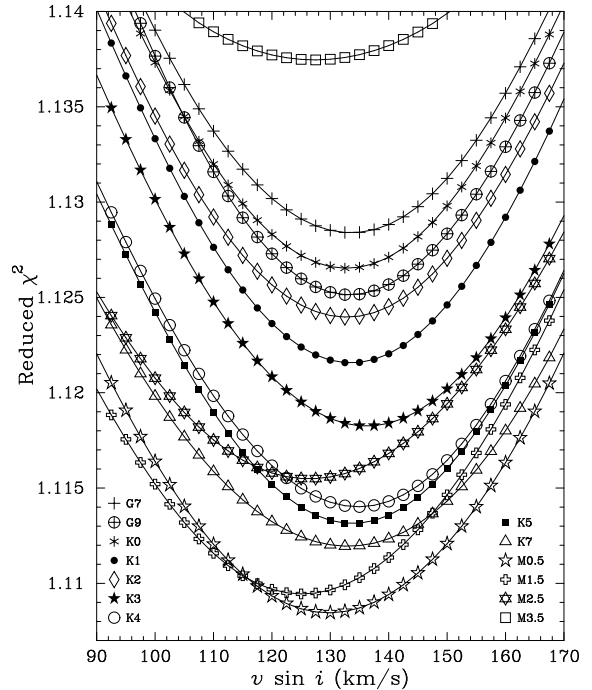


**Figure 9.** Determination of  $v \sin i$  for V347 Pup using different spectral-type templates. Degrees of freedom = 699.

### 3.8 The $K_R$ correction

The irradiation of the secondary stars in CVs by the emission regions around the white dwarf and the bright spot has been shown to influence the measured  $K_R$  (e.g. Wade & Horne 1988, Watson & Dhillon 2001). For example, if absorption lines are quenched on the irradiated side

of the secondary, the centre of light will be shifted towards the back of the star. The measured  $K_R$  will then be larger than the true (dynamical) value.

Diaz & Hubeny (1999) found evidence for irradiation of the secondary star in V347 Pup, leading them to apply a correction to their measured  $K_R$  value. This fact, and the presence of Balmer and HeI emission from the inner face of the secondary star seen in the Doppler maps and trailed spectra (Section 3.4), prompted us to look for similar irradiation effects in the absorption lines of our data. We applied the following two observational tests. First, the rotationally broadened line profile would be distorted if there was a non-uniform absorption distribution across the surface of the secondary star (Davey & Smith 1992). This would result in a non-sinusoidal radial velocity curve. Second, one would expect a depletion of secondary star absorption-line flux at phase 0.5, where the quenched inner-hemisphere is pointed towards the observer (e.g. Friend et al. 1990).

The secondary star radial velocity curves were produced by cross-correlating the V347 Pup spectra with the best-fitting smeared and broadened template spectra, as described in Section 3.6. The cross-correlation peaks were plotted against phase to produce the radial velocity curves shown in the lower panel of Fig. 10. There is evidence for an eccentricity in the radial velocity curve compared with the sinusoidal fit represented by the thin solid line, although the data are noisy.

The variation of secondary star absorption-line flux with phase for V347 Pup is shown in the top panel of Fig. 10. These light curves were produced by optimally subtracting the smeared and rotationally broadened best-fitting template from the individual CV spectra (with the secondary radial velocity shifted out) as described in Section 3.7. This time, however, the spectra were continuum subtracted rather than normalised to ensure that the measurements were not affected by a fluctuating disc brightness. The constants produced by the optimal subtraction are secondary star absorption-line fluxes, correct relative to each other, but not in an absolute sense. The dashed lines super-imposed on the light curves represent the variation of flux with phase for a Roche lobe with a uniform absorption distribution. The sinusoidal nature is the result of the changing projected area of the Roche lobe through the orbit. The V347 Pup light curve is clearly not represented by a uniform Roche lobe distribution as the secondary star absorption-line flux vanishes between phases 0.4–0.6.

These three pieces of evidence, as well as the disappearance of the CCFs between phases 0.4–0.6 seen in Fig. 7 suggest that the secondary star in V347 Pup is irradiated and we must correct the  $K_R$  values accordingly.

It is possible to correct  $K_R$  for the effects of irradiation by modelling the secondary star flux distribution. In our simple model, we divided the secondary Roche lobe into 40 vertical slices of equal width from the  $L_1$  point to the back of the star. We then produced a series of model light curves (using the system parameters derived in Section 3.10), varying the numbers of slices omitted from the inner hemisphere of the secondary which contribute to the total flux. The model light curves were then scaled to match the observed data, and the best-fitting model found by measuring the  $\chi^2$  between the two. In all models, we used a gravity-darkening parameter  $\beta = 0.08$  and limb-darkening

coefficient  $u = 0.5$  (e.g. Watson & Dhillon 2001). The negative data points around phase 0.5 were set to zero, as the secondary star absorption line flux disappears at this point. Once the best-fitting light curve was found, we produced fake V347 Pup spectra from the model, which were cross-correlated with a fake template star to produce a synthetic radial velocity curve. In the first instance, the synthetic curve mimicked the non-sinusoidal nature of the observed data, but with a larger semi-amplitude. This was expected, as the model input parameters used the uncorrected  $K_R$  derived in Section 3.10. We then lowered  $K_R$  and repeated the process, until the semi-amplitude of the model and observed radial velocity curves were in agreement, each time checking the light curve models for goodness of fit. The resulting  $K_R$  was then adopted as the real (or dynamical)  $K_R$  value.

The best-fitting model light curve was produced by omitting 12 slices when fitting the data (reduced  $\chi^2$  between model and data = 1.03). The model light curves omitting 11, 12 and 13 slices are shown by the solid lines in Fig. 10. Our final model, which has an input  $K_R$  of 198 km s<sup>-1</sup>, produces the radial velocity curve shown as the thick solid line in the lower panel of Fig. 10. There is good agreement between this and the observed data. If gravity-darkening and limb-darkening are neglected, the best fit light curve remains the same, but produce a  $K_R$  value which is  $\sim 6$  km s<sup>-1</sup> lower.

In summary, we correct the  $K_R$  of V347 Pup from 216 km s<sup>-1</sup> to 198 km s<sup>-1</sup>. This correction of 18 km s<sup>-1</sup> is exactly the same as that calculated by Diaz & Hubeny (1999) using a much simpler approximation, which changed their measured value of 205 km s<sup>-1</sup> to 187 km s<sup>-1</sup>.

### 3.9 The distance to V347 Pup

By finding the apparent magnitude of the secondary star from its contribution to the total light of the system, and estimating its absolute magnitude, we can calculate the distance ( $d$ ) using the equation:

$$5 \log(d/10) = m_V - M_V - d A_V/1000 \quad (4)$$

where  $A_V$  is the visual interstellar extinction in magnitudes per kpc.

The mean  $R$ -band photometric flux of V347 Pup during the recorded spectra is 8.93 mJy, which we convert to a mean  $R$ -band magnitude of  $13.8 \pm 0.3$ . The uncertainty reflects the change in brightness of the system between 25 and 27 Dec. During this time, the secondary star contributes  $13 \pm 2$  per cent of the total light of the system, assuming an early M spectral type (see Table 4). The apparent magnitude of the secondary is therefore  $R = 16.0 \pm 0.4$ , which we convert to a  $V$ -band magnitude of  $17.3 \pm 0.4$  using a typical  $V - R$  value for an early M star from Gray (1992). There are a number of ways of estimating the absolute magnitude of the secondary star, assuming it is on the main sequence (e.g. Patterson 1984; Warner 1995b; Gray 1992). We took each of these into account and adopt an average value of  $M_V = +8.8 \pm 0.5$ . Mauche et al. (1994) estimated the extinction to V347 Pup to be  $E(B - V) = 0.05$ , which results in  $A_V = 0.16$  (Scheffler 1982). The distance to V347 Pup is calculated from equation 4 to be  $490 \pm 130$  pc.

Buckley et al. (1990) estimate the distance to V347 Pup to be between 174–380 pc, based on their

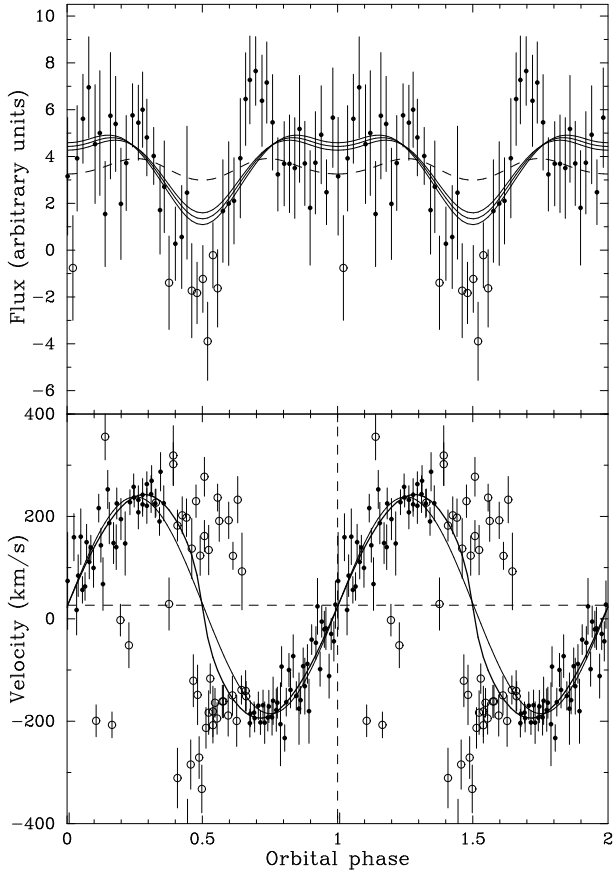


**Figure 10.** Upper panel: Secondary star absorption line light curve with model fits (solid lines). Model fits are shown for Roche lobes with 11, 12 and 13 slices removed (see text for details). The lower the line, the more slices removed. The dashed line represents a model where 0 slices have been removed. The data have been phase-binned into 50 bins to increase S/N. Lower panel: Measured secondary star radial velocity curve with a sinusoidal fit (thin solid line) and the best-fitting model fit (thick solid line). In both panels, the open circles indicate points that have been omitted from the fits and the data have been folded to show 2 orbital phases.

measured system inclination and out-of-eclipse magnitude. Mauche et al. (1994) use their interstellar reddening measurement and a mean interstellar hydrogen number density to estimate a distance of 340–590 pc. Finally, Diaz & Hubeny (1999) find a distance of  $510 \pm 160$  pc from the spectral line depths of the secondary star. Our value is consistent with all distance estimates in the literature.

### 3.10 System parameters

Using the  $K_R$  and  $v \sin i$  values found in Sections 3.7 and 3.8 in conjunction with the period determined in Section 3.1 and a measurement of the eclipse full-width at half depth ( $\Delta\phi_{1/2}$ ), we can calculate accurate system parameters for V347 Pup.

In order to determine  $\Delta\phi_{1/2}$ , we estimated the flux out of eclipse (the principal source of error) and at eclipse minimum, and then measured the full-width of the eclipse half-width between these points. The eclipse full-width at half-

depth was measured to be  $\Delta\phi_{1/2} = 0.115 \pm 0.005$ , in agreement with the eclipse half-width at half-depth of  $0.052 \pm 0.002$  measured by Buckley et al. (1990) at the  $2\sigma$  level.

We have opted for a Monte Carlo approach similar to Horne, Welsh & Wade (1993) to calculate the system parameters and their errors. For a given set of  $K_R$ ,  $v \sin i$ ,  $\Delta\phi_{1/2}$  and  $P$ , the other system parameters are calculated as follows.

$R_2/a$  can be estimated because we know that the secondary star fills its Roche lobe (as there is an accretion disc present and hence mass transfer).  $R_2$  is the equatorial radius of the secondary star and  $a$  is the binary separation. We used Eggleton’s formula (Eggleton 1983) which gives the volume-equivalent radius of the Roche lobe to better than 1 per cent, which is close to the equatorial radius of the secondary star as seen during eclipse,

$$\frac{R_2}{a} = \frac{0.49q^{2/3}}{0.6q^{2/3} + \ln(1 + q^{1/3})}. \quad (5)$$

The secondary star rotates synchronously with the orbital motion, so we can combine  $K_R$  and  $v \sin i$ , to get

$$\frac{R_2}{a}(1 + q) = \frac{v \sin i}{K_R}. \quad (6)$$

By considering the geometry of a point eclipse by a spherical body (e.g. Dhillon, Marsh & Jones 1991), the radius of the secondary can be shown to be

$$\left(\frac{R_2}{a}\right)^2 = \sin^2 \pi \Delta\phi_{1/2} + \cos^2 \pi \Delta\phi_{1/2} \cos^2 i, \quad (7)$$

which, using the value of  $R_2/a$  obtained using equations 5 and 6, allows us to calculate the inclination,  $i$ , of the system. The geometry of a disc eclipse can be approximated to a point eclipse if the light distribution around the white dwarf is axi-symmetric (e.g. Dhillon 1990). This approximation is justified given the symmetry of the primary eclipses in the photometry light curves (Fig. 2). Kepler’s Third Law gives us

$$\frac{K_R^3 P_{orb}}{2\pi G} = \frac{M_1 \sin^3 i}{(1 + q)^2}, \quad (8)$$

which, with the values of  $q$  and  $i$  calculated using equations 5, 6 and 7, gives the mass of the primary star. The mass of the secondary star can then be obtained using

$$M_2 = qM_1. \quad (9)$$

The radius of the secondary star is obtained from the equation

$$\frac{v \sin i}{R_2} = \frac{2\pi \sin i}{P}, \quad (10)$$

(e.g. Warner 1995a) and the separation of the components,  $a$ , is calculated from equations 6 and 10 with  $q$  and  $i$  now known.

The Monte Carlo simulation takes 10 000 values of  $K_R$ ,  $v \sin i$ , and  $\Delta\phi_{1/2}$  (the error on the period is deemed to be negligible in comparison to the errors on  $K_R$ ,  $v \sin i$ , and  $\Delta\phi_{1/2}$ ), treating each as being normally distributed about their measured values with standard deviations equal to the errors on the measurements. We then calculate the masses of the components, the inclination of the system, the radius of the secondary star, and the separation of the components, as

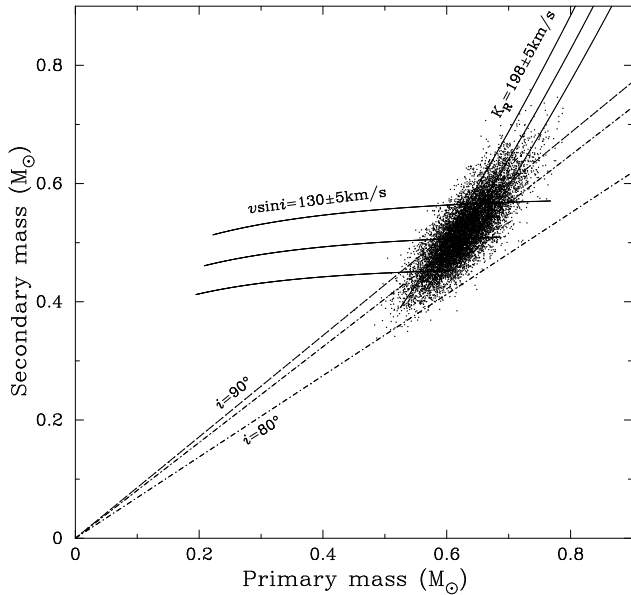


**Figure 11.** Monte Carlo determination of system parameters for V347 Pup. Each dot represents an  $M_1, M_2$  pair; the solid curves satisfy the  $v \sin i$  and  $K_R$  constraints, and the dashed lines mark lines of constant inclinations ( $i = 80^\circ, 85^\circ$  and  $90^\circ$ ).

outlined above, omitting ( $K_R, v \sin i, \Delta\phi_{1/2}$ ) triplets which are inconsistent with  $\sin i \leq 1$ . Each accepted  $M_1, M_2$  pair is then plotted as a point in Figure 11, and the masses and their errors are computed from the mean and standard deviation of the distribution of these pairs.

We find the component masses of V347 Pup to be  $M_1 = 0.63 \pm 0.04 M_\odot$  and  $M_2 = 0.52 \pm 0.06 M_\odot$ . The values of all the system parameters deduced from the Monte Carlo computation are listed in Table 5, including  $K_R$ -corrected and non  $K_R$ -corrected values for comparison. Note that our derived  $K_W$  of  $163 \pm 9 \text{ km s}^{-1}$  is in remarkable agreement with the  $K_W$  values of Still, Buckley & Garlick (1998) who measure  $156 \pm 10 \text{ km s}^{-1}$  using a double-Gaussian convolution of the Balmer lines, and  $166 \text{ km s}^{-1}$  as the centre of axisymmetric Balmer emission. The white dwarf mass of  $0.63 \pm 0.04 M_\odot$  is consistent with the average value of  $\bar{M}_1 = 0.80 \pm 0.22 M_\odot$  (for CVs above the period gap) determined by Smith & Dhillon (1998). The empirical relation obtained by Smith & Dhillon (1998) between mass and radius for the secondary stars in CVs predicts that if the secondary star in V347 Pup is on the main-sequence, it should have a radius of  $0.54 \pm 0.08 R_\odot$ . Our measured value of  $0.60 \pm 0.02 R_\odot$  (from equation 10) is consistent with this value.

## 4 DISCUSSION

### 4.1 Spiral arms

Spiral-armed disc asymmetries are evident in the HeI and H $\beta$  Doppler maps, confirming the findings of Still, Buckley & Garlick (1998) in their H $\beta$  and H $\gamma$  maps. Similar spiral structures have been observed in dwarf novae during outburst (e.g. IP Peg, Steeghs, Harlaftis & Horne 1997; U Gem, Groot, Rutten & van Paradijs 2001). Tidally driven

spiral density waves can develop in accretion discs due to the tidal torque of the mass donor star on the outer disc (Sawada, Matsuda & Hachisu 1986, Blondin 2000, Boffin 2001). Their detection in outburst only reflects the much stronger tidal effects on the accretion disc when it increases in size and temperature during outburst, in which case a tidally induced spiral structure is expected that closely matches the observed structures (Armitage & Murray 1998, Steeghs & Stehle 1999, Steeghs 2001). In dwarf novae, these asymmetries decay as the system returns to quiescence, and the disc cools and shrinks. In order for a similar tidal response to be responsible for the disc asymmetry in V347 Pup, its disc must be large and comparable to the tidal radius. We calculate the tidal radius of the accretion disc to be  $0.33a$  using the pressureless disc models of Paczyński (1977) and our new system parameters. The measured disc radius of  $R_D/a = 0.28 \pm 0.03$  is comparable in size to the tidal radius, and therefore consistent with a tidal origin for the observed spiral structure.

Our observations show that the spiral structures are clearly visible in the HeI Doppler maps, but are either weak or non-existent in the Balmer and HeII maps. This is in contrast to dwarf novae in outburst, which typically show stronger spiral structures in the HeII and Balmer lines (e.g. Marsh 2001; Morales-Rueda 2004). This could be a reflection of different densities and temperatures in NL discs compared to the discs of dwarf novae in outburst, or it could simply be due to a contrast effect where the relative contribution of the spiral structure is not as high in the HeII and Balmer maps due to the presence of low-velocity emission.

Note that the impact of such tidally-induced spiral arms on the angular momentum transport has not been fully established. If they are associated with hydrodynamical shocks, such as in the simulations of Sawada, Matsuda & Hachisu (1986), their contribution to the angular momentum transport could be very significant. On the other hand, Smak (2001) and Ogilvie (2002) propose that these disc structures may reflect tidally thickened areas in the outer disc as it expands close to its tidal radius. Their enhanced emission is then caused by irradiation from the accreting white dwarf and regions close to it.

The prospect of testing such basic disc physics with observations warrants the study of these disc structures in more detail (see also Morales-Rueda 2004). With V347 Pup, we have a target that appears to have a persistent disc asymmetry that is more accessible than the transient spiral structure observed in dwarf novae.

### 4.2 Mass transfer stability

The mass ratio of a CV is of great significance, as it governs the properties of mass transfer from the secondary to the white dwarf primary. This in turn governs the evolution and behaviour of the system.

The secondary star responds to mass loss on two timescales. First, the star returns to hydrostatic equilibrium on the dynamical timescale, which is the sound-crossing time of the region affected. Second, the star settles into a new thermal equilibrium configuration on a thermal timescale.

The two timescales upon which the secondary responds to mass loss leads to two types of mass transfer instability.

**Table 5.** System parameters for V347 Pup. The Monte Carlo results for corrected and uncorrected  $K_R$  values are shown for comparison. The radial velocity of the white dwarf ( $K_W$ ) has also been calculated from the secondary star parameters.

Parameter	Non $K_R$ -corrected		$K_R$ -corrected	
	Measured Value	Monte Carlo Value	Measured Value	Monte Carlo Value
$P_{orb}$ (d)	0.231936060		0.231936060	
$K_R$ (km s $^{-1}$ )	$216 \pm 5$	$215 \pm 5$	$198 \pm 5$	$198 \pm 5$
$v \sin i$ (km s $^{-1}$ )	$130 \pm 5$	$131 \pm 5$	$130 \pm 5$	$131 \pm 5$
$\Delta\phi_{1/2}$	$0.115 \pm 0.005$	$0.111 \pm 0.003$	$0.115 \pm 0.005$	$0.113 \pm 0.004$
$q$		$0.73 \pm 0.05$		$0.83 \pm 0.05$
$i^\circ$		$85.0 \pm 2.1$		$84.0 \pm 2.3$
$K_W$ (km s $^{-1}$ )		$158 \pm 9$		$163 \pm 9$
$M_1/M_\odot$		$0.73 \pm 0.05$		$0.63 \pm 0.04$
$M_2/M_\odot$		$0.54 \pm 0.06$		$0.52 \pm 0.06$
$R_2/R_\odot$		$0.60 \pm 0.02$		$0.60 \pm 0.02$
$a/R_\odot$		$1.72 \pm 0.04$		$1.66 \pm 0.05$
$d$ (pc)	$490 \pm 130$		$490 \pm 130$	
Spectral type of secondary	M0.5 V		M0.5 V	
$\Delta\phi$	$0.110 \pm 0.005$		$0.110 \pm 0.005$	
$R_D/R_1$		$0.72 \pm 0.08$		$0.72 \pm 0.09$

If, upon mass loss, the dynamical response of the secondary is to expand relative to the Roche lobe, mass transfer is dynamically unstable and mass transfer proceeds on the dynamical timescale. Politano (1996) made an analytic fit to the models of Hjellming (1989) to give the limit of dynamically stable mass loss, plotted as the solid line in Fig. 12. Dynamically stable mass transfer can occur if the CV lies below this line. This limit is important for low mass secondary stars ( $M_2 < 0.5M_\odot$ ), as they have significant convective envelopes that tend to expand adiabatically in response to mass loss (de Kool 1992).

Thermally unstable mass transfer is possible if the dynamic response of the star to mass loss is to shrink relative to its Roche lobe (i.e. mass transfer is *dynamically stable*). This occurs at high donor masses ( $M_2 > 0.8M_\odot$ ) when the star has a negligible convective envelope and its adiabatic response to mass loss is to shrink. (e.g. de Kool 1992; Politano 1996). Mass transfer then initially breaks contact and the star begins to settle into its new thermal equilibrium configuration. If the star's thermal equilibrium radius is now bigger than the Roche lobe, mass transfer is again unstable, but proceeds on the slower, thermal timescale. The limit of thermally-stable mass transfer can be found by differentiating the main-sequence mass-radius relationship given in Politano (1996). Thermally-stable mass transfer can occur if the CV appears below the dotted line plotted in Fig. 12.

The limit for dynamically stable mass transfer is important in the case of V347 Pup owing to the low secondary star mass. Fig. 12 shows that the system is just consistent with the limit at the  $1\sigma$  level. The mass transfer stability limits, however, are true only for ZAMS stars, whereas the secondary stars in CVs are expected to have undergone some evolution. The loss of the outer envelope, for example, would result in a larger than normal helium to hydrogen ratio and affect the star's response to mass loss. For instance, DX And, which lies outside the limit, has been shown to have an evolved companion (Drew, Jones & Woods 1993).

There is tentative evidence that the secondary star in V347 Pup is evolved by considering three pieces of evidence. First, V347 Pup falls outside the limit for dynamically stable mass transfer (although agrees at the  $1\sigma$  level). Second, the measured radius is at the upper limit for a main-sequence companion of the same mass (Smith & Dhillon 1998). Third, the secondary star mass and spectral type measured for V347 Pup are closer to the evolved models of Kolb, King & Baraffe (2001) than the ZAMS models.

## 5 CONCLUSIONS

(i) We have measured the radial and rotational velocities of the secondary star in V347 Pup in order to calculate the component masses and other system parameters. The secondary star radial velocity is affected by irradiation from the emission regions around the primary, which we correct for using a model. We find the component masses in V347 Pup to be  $M_1 = 0.63 \pm 0.04 M_\odot$  for the white dwarf primary and  $M_2 = 0.52 \pm 0.06 M_\odot$  for the M0.5V secondary star. V347 Pup shows many of the characteristics of the SW Sex stars, exhibiting single-peaked emission lines, high-velocity S-wave components and phase-offsets in the radial velocity curves.

(ii) V347 Pup lies outside the theoretical limit for dynamically stable mass transfer in ZAMS stars, but is just consistent at the  $1\sigma$  uncertainty level. This piece of evidence, together with a secondary star radius at the upper limit for a main-sequence companion of the same mass, suggests that the secondary star in V347 Pup may be evolved. Additionally, the secondary star mass and spectral type measured for V347 Pup are closer to the evolved models of Kolb, King & Baraffe (2001) than the ZAMS models.

(iii) The presence of spiral arms in the accretion disc, first noted by Still, Buckley & Garlick (1998), has been con-

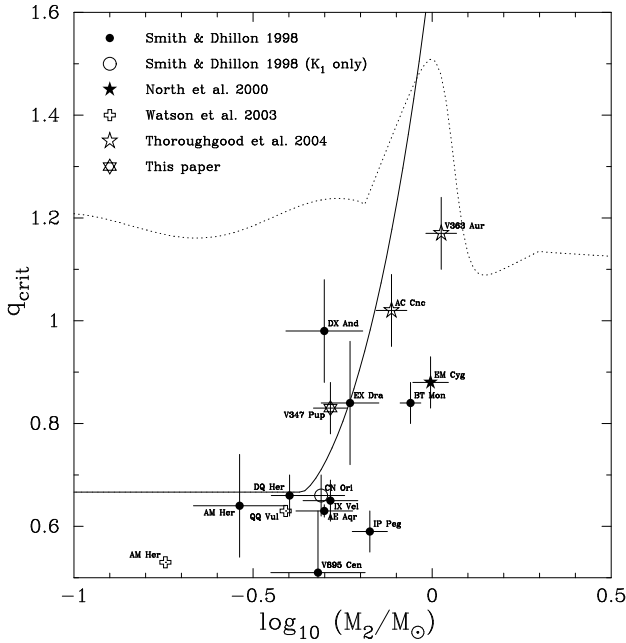


**Figure 12.** Critical mass ratios for mass transfer stability. The dotted line represents the condition for thermal instability; the solid line represents the condition for dynamical instability (Politano 1996). Both curves assume the star is initially in thermal equilibrium. Mass ratios and secondary masses from the compilation of Smith & Dhillon (1998), North et al. (2000), Watson et al. (2003), and Thoroughgood et al. (2004) are over-plotted. The mass ratios and secondary star masses of V347 Pup determined in this paper are also plotted.

firmed. Consistent with this, we find that the measured accretion disc radius is close to the tidal radius computed from the pressureless disc models of Paczyński (1977). The persistent spiral arms seen in this bright novalike makes it an excellent candidate in which to study these features, rather than the transient spiral structures observed in dwarf novae.

## ACKNOWLEDGEMENTS

TDT is supported by a PPARC studentship; CAW is supported by PPARC grant number PPA/G/S/2000/00598; SPL is supported by PPARC. DS acknowledges a Smithsonian Astrophysical Observatory Clay Fellowship.

## REFERENCES

Armitage P. J., Murray J. R., 1998, *MNRAS*, 297, L81  
 Baptista R., Cieslinski D., 1991, *IAU Circ.*, 5407  
 Blondin J. M., 2000, *New Astronomy*, 5, 53  
 Boffin H. M. J., 2001, in Boffin H., Steeghs D., Cuypers J., eds, *Proceedings of the International Workshop on Astro-tomography*, Brussels, July 2000. Springer-Verlag Lecture Notes in Physics, Dusseldorf, p. 69  
 Buckley D. A. H., Sullivan D. J., Remillard R. A., Tuohy I. R., Clark M., 1990, *ApJ*, 355, 617  
 Davey S. C., Smith R. C., 1992, *MNRAS*, 257, 476  
 de Kool M., 1992, *AA*, 261, 188  
 Dhillon V. S., Jones D. H. P., Marsh T. R., 1994, *MNRAS*, 266, 859

Dhillon V. S., Marsh T. R., Jones D. H. P., 1991, *MNRAS*, 252, 342  
 Dhillon V. S., Marsh T. R., Jones D. H. P., 1997, *MNRAS*, 291, 694  
 Dhillon V. S., Marsh T. R., Jones D. H. P., Smith R. C., 1992, *MNRAS*, 258, 225  
 Dhillon V. S., 1990, D. Phil thesis, University of Sussex  
 Diaz M. P., Hubeny I., 1999, *ApJ*, 523, 786  
 Drew J. E., Jones D. H. P., Woods J. A., 1993, *MNRAS*, 260, 803  
 Eggleton P. P., 1983, *ApJ*, 268, 368  
 Friend M. T., Martin J. S., Smith R. C., Jones D. H. P., 1990, *MNRAS*, 246, 637  
 Gray D. F., 1992, *The Observation and Analysis of Stellar Photospheres*. Cambridge University Press, Cambridge  
 Groot P. J., Rutten R. G. M., van Paradijs J., 2001, *AA*, 368, 183  
 Harrop-Allin M. K., Warner B., 1996, *MNRAS*, 279, 219  
 Hjellming M. S., 1989, PhD thesis, University of Illinois  
 Honeycutt R. K., 2001, *PASP*, 113, 473  
 Horne K., Marsh T. R., 1986, *MNRAS*, 218, 761  
 Horne K., Welsh W. F., Wade R. A., 1993, *ApJ*, 410, 357  
 Knigge C., Long K. S., Hoard D. W., Szkody P., Dhillon V. S., 2000, *ApJ*, 539, L49  
 Kolb U., King A. R., Baraffe I., 2001, *MNRAS*, 321, 544  
 Marsh T. R., Horne K., 1988, *MNRAS*, 235, 269  
 Marsh T. R., 1988, *MNRAS*, 231, 1117  
 Marsh T. R., 2001, in Boffin H., Steeghs D., Cuypers J., eds, *Proceedings of the International Workshop on Astro-tomography*, Brussels, July 2000. Springer-Verlag Lecture Notes in Physics, Dusseldorf, p. 1  
 Mason E., Howell S. B., 2003, *AA*, 403, 699  
 Mauche C. W., Raymond J. C., Buckley D. A. H., Mouchet M., Bonnell J., Sullivan D. J., Bonnet-Bidaud J., Bunk W. H., 1994, *ApJ*, 424, 347  
 Morales-Rueda L., 2004, *Astron. Nach.*, 325, 193  
 North R. C., Marsh T. R., Moran C. K. J., Kolb U., Smith R. C., Stehle R., 2000, *MNRAS*, 313, 383  
 Ogilvie G. I., 2002, *MNRAS*, 330, 937  
 Paczyński B., 1977, *ApJ*, 216, 822  
 Patterson J., 1984, *ApJS*, 54, 443  
 Politano M., 1996, *ApJ*, 465, 338  
 Rappaport S., Verbunt F., Joss P. C., 1983, *ApJ*, 275, 713  
 Sawada K., Matsuda T., Hachisu I., 1986, *MNRAS*, 219, 75  
 Scheffler H. in Schaifers K., Voigt H. H., eds, *Landolt-Börnstein Numerical Data and Functional Relationships in Science and Technology*, New Series, Group VI, Vol. 2, Subvol. c, p. 47, Springer Verlag, Heidelberg, 1982  
 Schneider D. P., Young P. J., 1980, *ApJ*, 238, 946  
 Shafter A. W., Hessman F. V., Zhang E. H., 1988, *ApJ*, 327, 248  
 Shafter A. W., Szkody P., Thorstensen J. R., 1986, *ApJ*, 308, 765  
 Shlosman I., Vitello P., Mauche C. W., 1996, *ApJ*, 461, 377  
 Skilling J., Bryan R. K., 1984, *MNRAS*, 211, 111  
 Smak J. I., 2001, *Acta Astron.*, 51, 295  
 Smith D. A., Dhillon V. S., 1998, *MNRAS*, 301, 767  
 Smith D. A., Dhillon V. S., Marsh T. R., 1998, *MNRAS*, 296, 465  
 Spruit H. C., Ritter H., 1983, *AA*, 124, 267  
 Steeghs D., Stehle R., 1999, *MNRAS*, 307, 99  
 Steeghs D., Harlaftis E. T., Horne K., 1997, *MNRAS*, 290, 28L  
 Steeghs D., 2001, in Boffin H., Steeghs D., Cuypers J., eds, *Proceedings of the International Workshop on Astro-tomography*, Brussels, July 2000. Springer-Verlag Lecture Notes in Physics, Dusseldorf, p. 45  
 Steeghs D., 2003, *MNRAS*, 344, 448  
 Still M. D., Buckley D. A. H., Garlick M. A., 1998, *MNRAS*, 299, 545

- Still M. D., Dhillon V. S., Jones D. H. P., 1995, *MNRAS*, 273, 863
- Thoroughgood T. D., Dhillon V. S., Littlefair S. P., Marsh T. R., Smith D. A., 2001, *MNRAS*, 327, 1323
- Thoroughgood T. D., Dhillon V. S., Watson C. A., Buckley D. A. H., Steeghs D., Stevenson M. J., 2004, *MNRAS*, 353, 1135
- Vande Putte D., Smith R. C., Hawkins N. A., Martin J. S., 2003, *MNRAS*, 342, 151
- Wade R. A., Horne K., 1988, *ApJ*, 324, 411
- Warner B., 1995a, *Cataclysmic Variable Stars*. Cambridge University Press, Cambridge
- Warner B., 1995b, *Ap&SS*, 232, 89
- Watson C. A., Dhillon V. S., 2001, *MNRAS*, 326, 67
- Watson C. A., Dhillon V. S., Rutten R. G. M., Schwope A. D., 2003, *MNRAS*, 341, 129